TU Delft

Delft University of Technology

Waste glass as partial mineral precursor in alkali-activated slag/fly ash system

Zhang, Shizhe; Keulen, Arno; Arbi Ghanmi, K.; Ye, Guang

DOI
10.1016/j.cemconres.2017.08.012

Publication date
2017

Document Version
Accepted author manuscript

Published in
Cement and Concrete Research

Citation (APA)
Zhang, S., Keulen, A., Arbi Ghanmi, K., & Ye, G. (2017). Waste glass as partial mineral precursor in alkali-activated slag/fly ash system. *Cement and Concrete Research*, *102*, 29-40. https://doi.org/10.1016/j.cemconres.2017.08.012

Important note
To cite this publication, please use the final published version (if applicable).
Please check the document version above.

Copyright
Other than for strictly personal use, it is not permitted to download, forward or distribute the text or part of it, without the consent of the author(s) and/or copyright holder(s), unless the work is under an open content license such as Creative Commons.

Takedown policy
Please contact us and provide details if you believe this document breaches copyrights.
We will remove access to the work immediately and investigate your claim.

This work is downloaded from Delft University of Technology.
For technical reasons the number of authors shown on this cover page is limited to a maximum of 10.

Waste glass as partial mineral precursor in alkali-activated slag/fly ash system

Shizhe Zhang[1*], Arno Keulen[2,3], Kamel Arbi[1], Guang Ye[1]

[1] Microlab, Section Materials and Environment, Faculty of Civil Engineering and Geosciences, Delft University of Technology, Stevinweg 1, 2628 CN, Delft, the Netherlands

[2] Van Gansewinkel Minerals, Flight Forum 240, 5657 DH, Eindhoven, the Netherlands

[3] Department of the Built Environment, Eindhoven University of Technology, P.O. Box 513, 5600 MB, Eindhoven, the Netherlands

* Corresponding author e-mail: Shizhe.Zhang@tudelft.nl,

Abstract

The feasibility of a waste glass powder residue (GP) from glass recycling as partial mineral precursor to produce alkali-activated materials is investigated. GP served as powder coal fly ash (PCFA) replacement within a reference system composed of 50% PCFA and 50% ground granulated blast furnace slag (GGBS). Compared with PCFA, GP was better involved in the alkali activation process by having a higher silica and Ca dissolution. Furthermore, increasing GP replacement up to 30% prolonged the induction period, facilitated the gel formation and yielded a 35% higher 28-day compressive strength. These observations are similar to the effect of using both sodium hydroxide and sodium silicate as alkali activator in alkali-activated slag/fly ash systems. A higher polymerization of the gel network was also observed. Microstructure analysis indicated that the main reaction product is a calcium silicate hydrate type gel substituted with Al and Na (C-(N)-A-S-H type gel).

This work largely contributes to the understanding of the reactivity and potential of GP and promotes its practical utilization as a mineral precursor in the production of alkaline cements.

Keywords: Waste glass; Alkali activated material; Microstructure; Fly ash; Slag

1 Introduction

Fast growing world population and its related industrialization have raised concerns about the environmental consequences of waste handling. Nowadays, many industries have started investing in optimization of waste disposal management systems to fulfill the national and international legislations. The development of a circular economy of mineral waste materials within the Netherlands and the European Union (EU) has been found to be highly potential and economical profitable. The potential waste materials are promoted to be recycled and re-used as primary or secondary raw materials in other industrial processes to lower their negative environmental impacts and preserve natural resources.

Within glass industry, the glass recycling has reached a relatively high average rate (>70% in the EU and >90% in the Netherlands) [1]. However, there are still some challenges related to non-recyclable glass fraction which does not meet the criteria for reuse in the production process of new glass. About 20,000 tons/year of such glass residue (glass powder and glass granular) are produced in the Netherlands [2] and most of this waste is sent to landfills. One possible solution for managing this waste glass fraction is to use it as a solid precursor in building materials. Previous studies [3-5] have already shown attempts to incorporate glass fractions into Ordinary Portland cement (OPC) concrete, with general focus on replacement of fine aggregate. However, their use as supplementary cementitious materials (SCMs) in OPC concrete is still scarce.

In recent decades, alkaline activation technology has emerged as an effective tool able to use different wastes and industrial by-products as solid precursors to produce cementitious materials. Compared with OPC, alkali activated materials (AAMs) offer a large reduction in CO_2

53 emissions (up to 80%) [6] and have comparable or better performance (such as high
54 mechanical strength at early ages, high stability in aggressive environments and resistance to
55 elevated temperatures). Fly ash and blast furnace slag are currently the most intensively used
56 solid precursors to produce alkali activated cement/concrete [7-10]. Many researchers have
57 found that the binary system of alkali-activated slag/fly ash has an improved mechanical
58 properties and durability [11-13]. The enhanced mechanical performance and durability of
59 alkali-activated slag/fly ash have attracted great attention by both scientific community and
60 construction industry. The previous studies on alkali-activated slag/fly ash are mostly on the
61 microstructure and mechanical properties, as well as some efforts on understanding the
62 chemical makeup and formation mechanism of the reaction products [10, 14, 15].
63 To our best knowledge, studies on using waste glass in alkali-activated slag/fly ash systems
64 are still rare. Only few studies dealing with waste glass as precursor in AAMs can be found in
65 the literature. For instance, Tashima et al. [16] investigated the properties and microstructure
66 of glass fiber waste activated by alkaline metal sodium (Na) and potassium (K) solutions. A
67 compressive strength of 77 MPa was found for mortars activated by 10M NaOH solution and
68 cured for 3 day at 65°C. Pascual et al. [17] used metakaolin (MK) to replace a part of the GP to
69 introduce Al and also to stabilize alkali ions in the system and observed increment of the
70 compressive strength with MK content of up to 8%. In contrast, the compressive strength
71 decreased when the content of the MK was lower than 3%. Redden et al. [18] reported that
72 NaOH activated GP provides higher compressive strength than NaOH activated fly ash.
73 Through microstructural analysis, they observed that the main reaction product was a sodium
74 silicate gel in alkali activated GP, while a combination of sodium silicate and sodium

75 aluminosilicate (N-A-S-H) gels was identified in GP-fly ash blends. Torres-Carrasco et al. [19,
76 20] investigated the possible use of waste glass as an activator in alkali activated slag mortar
77 and found that using NaOH/Na_2CO_3 and glass mixture solution as activator increases the
78 compressive strength.
79 This work presents an investigation on the utilization of waste glass as partial mineral
80 precursor in alkali-activated slag/fly ash systems for production of alkaline cements. The main
81 aim is to valorize this kind of waste to enlarge its utilization in other industrial processes and
82 to promote a sustainable construction.
83

2 Materials and methods

2.1 Materials

The mineral precursors used in this study are a granulated blast furnace slag (GGBS), a class F powder coal fly ash (PCFA) according to ASTM C 618 and a waste glass powder (GP) residue fraction supplied by Van Gansewinkel Maltha, the Netherlands. Unlike ordinary GP which is manufactured by crushing and grinding, this fine GP residue fraction is collected during the bottle glass recycling process. Material density for GGBS, PCFA and GP are 2890 kg/m^3, 2440 kg/m^3 and 2174 kg/m^3, respectively. Their particle size distribution curves are shown in Figure 1, with d50 particle size to be 17.88 µm for GGBS, 33.19 µm for PCFA and 5.07 µm for GP. Chemical compositions of all precursors were determined by X-ray fluorescence (XRF) considering the loss on ignition (LOI) at 950 ℃ and is shown in Table 1.

The alkaline activator solution was prepared by dissolving NaOH pellets (analytical grade, purity≥98%) in distilled water. The selected NaOH concentration is 4M, which is defined to be optimal taking into account the fresh and hardened performance of alkali activated GGBS/PCFA system [21-24] as well as the final costs.

2.2 Methods

2.2.1 Mix design

The starting point was a reference mixture of 50% PCFA and 50% GGBS (named R). Through a partial replacement of PCFA by GP, 3 paste mixtures with 10%, 20%, and 30% of GP (named respectively G10, G20 and G30) were prepared. The mix design of 4 mixtures is shown in Table 2. To study different levels of GP to PCFA replacement as main variables, the liquid to solid (L/S) ratio was kept at 0.42 to maintain a suitable workability for all the investigated mixtures.

The solid precursors were firstly mixed for 5 min using a HOBART® mixer at a low speed. Alkaline activator solution was then added gradually and the batches were mixed for additional 5 min at a medium speed. The fresh pastes mixtures were cast in polystyrene prism molds (40 mm x 40 mm x 160 mm) and then compacted with a vibration table for four times (each time for 30 seconds) before finally sealed with a plastic foil. The samples were cured in a climate room (20 ℃ and ≥98% RH) until testing.

2.2.2 Testing Methods

The reactivity of both GP and PCFA were measured by chemical dissolution treatment as described elsewhere [25-27]. The solid minerals were dissolved in the concentrated acid solution and were afterwards treated with boiling potassium hydroxide solution. The obtained residue was rinsed, heated up to 950 ℃ and then was cooled to room temperature in a desiccator. The dissolved fraction corresponding to the mass loss after chemical dissolution treatment is determined as the amorphous phase content. The amount of reactive SiO_2 and Al_2O_3 was also calculated.

Element dissolution tests of PCFA and GP in alkali activator solution were performed following the modified NEN 7341 standard [25]. In total 5 g of mineral powder was added into 50 ml of NaOH solution and stirred at 300 rpm using a magnetic stirrer. For each precursor, different dissolution times were set as 5 min, 0.5 h, 1 h, 2 h, 6 h and 12 h. After these times, the solutions were separated from the remaining solids through vacuum filtration using a 45 µm glass micro-filter paper. The eluate was acidified with 5 vol.% nitric acid and diluted 100 times before the Si, Al, Ca concentrations were measured using an Optima 5300 DV inductively coupled plasma optical emission spectrometry (ICP-OES).

Mechanical properties and microstructural characterization tests were performed on paste samples cured for 1, 7, and 28 days as follows:

- Compressive strength was measured in accordance with NEN-196-1 [28] at 1, 7, and 28 days.
- X-ray diffraction (XRD) was conducted using a Philips PW 1830 powder X-ray diffractometer, with Cu Kα (1.5406 Å) radiation, tube setting to be 40 kV and 40 mA, a step size of 0.030 °, and a 2θ range of 5-70 °.
- Fourier transform infrared spectroscopy (FTIR) was performed using a Spectrum TM 100 Optical ATR-FTIR spectrometer over the wavelength range of 600 to 4000 cm^{-1} with a resolution of 1 cm^{-1}.
- Isothermal calorimetry was conducted using a TAM-Air-314 isothermal conduction calorimeter. Calibration was done at 20 ℃ before measurements, which lasted for a period of 120 h. The data were recorded every 1 min and two replicates for each mixture were measured.
- Differential thermogravimetry (DTG) was performed in a TG-449-F3-Jupiter instrument. The powder of samples was put in a small aluminum oxide crucible and heated from 40 ℃ to 1100 ℃ at 10 ℃/min in an argon protection atmosphere at a flow speed of 50 µL/min.
- Environmental scanning electron microscopy (ESEM), with energy dispersive X-ray (EDX) analysis, was performed using a Philips-XL30-ESEM. Samples were impregnated using an epoxy and were polished prior to ESEM analysis. The EDX was performed at an accelerating voltage of 20 kV. For 1, 7, and 28-day samples, 20 to 30 EDX measurements were conducted on R and G30 at each curing age.

3 Results and discussions

3.1 Precursor reactivity

3.1.1 Crystalline phases

The X-ray diffraction (XRD) patterns of GP, PCFA and GGBS are shown in Figure 2. The main crystalline phases in GP are quartz (SiO_2) and calcite ($CaCO_3$) while the minor phases are chamosite ($Fe_3Si_2O_5(OH)_4$), tobermorite ($Ca_5Si_6O_{16}(OH)_2$), and tremolite ($CaMg_3(SiO_4)_3$). These crystalline phases can be related to the initial ceramic particle contaminates within the input glass fraction. The PCFA crystalline phases are mainly quartz (SiO_2), mullite ($Al_6Si_2O_{13}$) and hematite (Fe_2O_3). In agreement with XRF results in Table 1, crystalline phases in GP and PCFA also show high SiO_2 contents. GGBS contains mainly amorphous phases. All precursors contain considerable amount of amorphous phases as can be reflected from the wide hump in the XRD patterns (from 17° to 35° for GP or PCFA and from 25° to 35° for GGBS). As the existence of abundant amorphous phases in GP is an indicator of reactivity, GP has the potential to be used as precursor to produce cementitious materials.

3.1.2 Reactive phases composition

It is commonly recognized that the reactivity of aluminosilicate precursors is proportional to the content of reactive SiO_2 and Al_2O_3. The presence of these elements is the key for developing the geopolymerization process and gel formation [29, 30]. The reactivity in this study is also represented by the amount of reactive SiO_2 and Al_2O_3 in the precursor.

The amorphous phase content and related reactive SiO_2 and Al_2O_3 content in GP and PCFA were obtained by analyzing their insoluble residue (I.R.) and soluble fractions derived from the chemical dissolution treatment. The reactive SiO_2, Al_2O_3 in GP and PCFA were calculated

using the corresponding chemical composition of original precursors (Table 1) and I.R. (Table 3) together with its related I.R. fraction. The reactive amount of each element was calculated using eq. (1):

$$\omega_{reactive}^{M-O} = \frac{m_{total} \times \omega_{total}^{M-O} - m_{residual} \times \omega_{residual}^{M-O}}{m_{total}} = \omega_{total}^{M-O} - \omega_{residual} \times \omega_{residual}^{M-O} \quad (1)$$

where M-O is SiO_2 or Al_2O_3, ω is the percentage (%) and m is the mass (g).

The obtained results on reactivity of GP and PCFA are presented in Table 4. The analysis shows that the amorphous content in GP is slightly higher (82%) than that in PCFA (77%). In addition, about 80% of the total SiO_2 was found to be reactive. However, a significant difference in the chemical composition was observed concerning Al_2O_3 and CaO. The reactive Al_2O_3 content in GP (0.92%) is extremely low compared to that in PCFA (27%). On the contrary, the total CaO content in GP (22%) is much higher, while PCFA only has very limited CaO content. These results clearly imply that GP serves as silica and calcium precursor that has low aluminum content. On the other hand, PCFA serves as silica and alumina precursor which is low in calcium. These inherent differences in reactivity may eventually influence the microstructure development of alkali-activated slag/fly ash with GP incorporation.

3.1.3 Solubility/dissolution rate

The element dissolution from mineral precursors is strongly related to their physical state and chemical composition. The results of reactivity experiments have already indicated clear differences between PCFA and GP and their reactive element composition. Dissolution experiments of both precursors over time were performed to provide further details on specific element release, which helps understanding the reaction kinetics and the early age

193 microstructure development. A quantitative analysis was carried out on dissolution kinetics
194 of element Si, Al, and Ca in 4M NaOH solutions, which is shown in Figure 3. It is worth noting
195 that the NaOH concentration is equal to that of the alkali-activator used in paste mixture
196 preparation.
197 The Si release rate of GP and PCFA shown in Figure 3(a) are relatively stable and roughly linear
198 within the first 12 h. GP tends to have a slightly higher dissolution rate as its reactive SiO_2
199 content is about 10% higher than PCFA, which results in a higher Si dissolution capacity. The
200 high rate Si solubility of GP could be also attributed to its smaller particle size [31].
201 The Al dissolution rate and concentration of PCFA shown in Figure 3(b) are much higher than
202 those of GP. This result is consistent with the reactivity of both precursors, since PCFA has
203 much higher reactive Al_2O_3 content than GP. Figure 3(c) indicates a higher rate and
204 concentration of Ca release in GP than PCFA, which is in agreement with its higher Ca content.
205 Both curves reach a plateau after 2 h, indicating a high dissolution kinetics of Ca from
206 precursors in high alkaline medium. Since the energy required for detachment of Ca from the
207 system is much lower than Al-O or Si-O bond energy, Ca as network modifier in the
208 aluminosilicate glass as well as Ca in the more depolymerized slag structures is known to
209 dissolve quickly via metal-proton exchange reactions in alkaline environment [32, 33]. This is
210 also the reason behind the fast early-age reaction kinetics of high Ca AAMs. It is observed that
211 the final dissolved Ca concentration is not proportional to the original Ca composition, which
212 is due to the reason that a part of the Ca from dissolution has been already consumed in
213 precipitation reactions forming ‘hydrated’ cementitious gel [34] or reincorporated in the
214 reacting surface of precursor [35].

3.1.4 Reaction heat of precursors

Isothermal calorimetry is conducted to evaluate the potential of NaOH activated precursors and their reaction kinetics, which can also reflect their reactivity. Figure 4(a) plots the heat flow of GGBS, PCFA and GP activated by 4M NaOH solution with an L/S ratio of 0.6 over the first 80 hours. Two sub-calorimetric peaks are observed in each curve: The first peak correlates with wetting and dissolution of the material. The second peak represents the reactions among dissolved species like Si, Al and Ca. From the heat flow rate in Figure 4(a), GGBS shows the highest reactivity while GP and PCFA only exhibit lower reactivity, although GP is slightly more reactive than PCFA. Additionally, their cumulative heat evolution in Figure 4(b) displays the same trend, where GGBS generates significantly the highest cumulative heat followed by GP and then PCFA. This trend is in line with previous studies indicating higher reactivity of GGBS compared with PCFA [36].

3.1.5 FTIR analysis

The reactivity of GP and PCFA have been analyzed by FTIR, which allows for monitoring the chemical bond changes induced by the precursor reaction. The spectra collected before chemical dissolution treatment is noted as ‘original’, while the spectra after treatment are noted as ‘residue’. The FTIR spectrum of dissolved amorphous phases were obtained by the subtraction of spectrum ‘residue’ from spectrum ‘original’ using OMNIC software [14]. The spectrum obtained from subtraction is referred as ‘dissolved’.

The FTIR spectra of original, residue and dissolved phases in GP are presented in Figure 5(a). Spectrum original of GP indicates a peak for quartz at 777 cm^{-1} [37]. Both the peak at 874 cm^{-1} and the relative broad hump at 1420 cm^{-1} are associated with the presence of carbonate (CO_3^{2-})

237 with different vibration modes: $v_2[CO_3]^{2-}$ for 874 cm^{-1} and $v_3[CO_3]^{2-}$ for 1420 cm^{-1} [38]. The
238 broad peak centered at approximately 1005 cm^{-1} is associated with asymmetric stretching of
239 Si-O-Si bonds. The stretching of Si-O-M (M being an alkali metal or alkali-earth metal) is found
240 at wavenumber 919 cm^{-1} [39]. Considering GP is rich in Ca, the wavenumber could be
241 associated with Si-O-Ca bonds. For the spectrum residue of GP, the peak at 965 cm^{-1} may be
242 associated with v_3(Si-O) stretching vibrations in SiO_4 tetrahedral. The existence peak may be
243 related to other crystalline Si phases like tremolite. For spectrum dissolved of GP, it is evident
244 that peaks at 1005 cm^{-1} and 919 cm^{-1} are mainly attributed to its reactive silica content.
245 The spectra of original, residue and dissolved phases in PCFA are plotted in Figure 5(b). The
246 peaks at 777 cm^{-1} and 796 cm^{-1} correspond to quartz. The main band at 1039 cm^{-1} represents
247 the Si/Al amorphous phases, which could be composed of high Al content [39]. For the
248 spectrum dissolved of PCFA, a huge drop of the broad hump at 1039 cm^{-1} is found after the
249 chemical dissolution treatment which is related to dissolution of high amounts of Si and Al
250 from the solid precursor. The two peaks near 800 cm^{-1} may be attributed to Si (Al)-O bonds or
251 Si-O-Al stretching bonds. The PCFA bonds at 1088 cm^{-1} and 1162 cm^{-1} are associated with
252 asymmetric stretching of (Si, Al)-O-Si of mullite phase.
253 The FTIR analysis of GP and PCFA shows that the reactive chemical bonds generally fall in the
254 range 1085-1092 cm^{-1}, 997-1001 cm^{-1} and 900-915 cm^{-1}, which mostly correspond to silicon
255 dominant structures (Si, Al^{IV})-O-Si bonds or (Si, Al^{IV})-O-M (M=Na or Ca) [40]. These bonds are
256 found to be highly reactive and largely determine the reactivity of aluminosilicate precursors
257 [40, 41].

3.2 Compressive strength

The compressive strength development of paste mixtures with increasing GP as PCFA replacement (from 0 to 30%) is shown in Figure 6. The 1-day strength is similar within all mixtures whereas compressive strength increases significantly at 7 and 28 days with higher amount of GP replacement. Compared with R (0% replacement), up to 35% strength gain is observed in G30 (30% GP as PCFA replacement). This increase could be attributed to the higher GP reactivity and availability of soluble silica provided by reaction between GP and NaOH, which facilitates the geopolymerization process and leads to higher amount of gel formation (Sections 3.3.3 and 3.3.4). In fact, the global activation process is comparable to the conjugational effect of using sodium silicate and sodium hydroxide as alkali activator (Section 3.3.3). Previous studies also confirmed that this conjugational effect results in additional available silica in the system and accelerates the gel polycondensation [42], which contributes to better mechanical properties.

Additionally, fly ash is known to contain 'hollow' cenospheres and plerospheres, which are prone to surface opening within dissolution process. Accordingly, the reaction products formation is assumed to be stimulated on the inner PCFA surface [43, 44]. This phenomenon has been also confirmed in PCFA cement paste blends, where reacted hollow PCFA particles provide extra space for the reaction products [45]. The opening of the 'closed' voids in PCFA was studied by alkaline solution treatment to substantiate that the PCFA in this study may also accommodate reaction products. A comparison of the pore structure between original and treated PCFA with 4M NaOH solutions for 2 h reveals obvious differences. As shown in Figure 7(a), the total porosity of the original ash was 5.69% and increased to 17.42% after

280 treatment. Additionally, Figure 7(b) indicates that the range of pore size broadens from 3-6
281 μm towards 2-10 μm after alkaline solution treatment. All these evidences suggest that the
282 surface opening of hollow PCFA may increase the accessibility of the finer pores and hence
283 promote the reaction products formation inside PCFA particles. However, these reaction
284 products formed inside the PCFA ineffectively contribute to the bonding of particles, which
285 leads to a decrease in compressive strength. This effect tends to be weakened with increasing
286 the GP content because of the reduced potential for the PCFA to accommodate reaction
287 products. Therefore, increasing the GP content eventually leads to increment of the
288 compressive strength.
289 However, a considerable strength decrement is found in G10 compared to R at 7 and 28 days,
290 which implies that different mechanisms are involved at low replacement levels. This
291 unexpected tendency may be induced by finer particle size distribution of GP compared with
292 PCFA. Smaller particle size of GP as well as its angular shape may have a negative influence on
293 the packing density of mixture [46], which could lead to a compressive strength decrease.
294 Meanwhile, the lower density of mixture with GP replacement may also contribute to the
295 strength decrement. It is worth noting that these effects are only dominant on the
296 compressive strength development at low GP replacement levels (⩽10%). With higher GP
297 replacement levels (⩾20%), the dominating factor may gradually change from the physical
298 effect to a chemical one. Compared with R mixture, only a minor increase of gel formation is
299 found in G10 while a significant increase is observed in G20 and G30 mixtures (will be
300 discussed in Section 3.3.4). Consequently, only the G10 reveals the strength decrease
301 compared to R at 7 and 28 days.

3.3 Microstructure Characterization

3.3.1 XRD analysis

The XRD patterns of samples after 1 day and 28 days curing are illustrated in Figure 8(a) and (b) respectively. At each curing age, the XRD spectra are stacked to investigate the effect of GP as PCFA replacement.

In all XRD patterns calcium silicate hydrate (C-S-H) phases ($1.5CaO{\cdot}SiO_2{\cdot}xH_2O$, PDF# 00-033-0306) are found near 29.4° which is in agreement with previous studies where C-S-H type gel was the main reaction product in slag dominated AAMs [8, 10, 12, 47, 48]. Considering the Al content in raw materials, this C-S-H type gel could have moderate Al incorporation into its structure. The abundance of C-S-H phases is found to increase with higher GP contents. As shown in Figure 8(b), the increase of GP replacement leads to a higher peak intensity of C-S-H phase. This may imply that the reaction kinetics and microstructure development are affected by GP replacement, which is in agreement with the observed difference in the reactivity and the element dissolution of both precursors (Section 3.1). It is believed that a higher amount of gel formation is achieved by increasing the GP content. To further validate such assumption, isothermal calorimetry and differential thermogravimetric analyses were carried out and the obtained results are further discussed in Sections 3.3.3. and 3.3.4.

Hydrotalcite ($Mg_6Al_2CO_3(OH)_{16}{\cdot}4H_2O$, PDF# 00-041-0191) is found at around 10.2° as the second main reaction product in all mixtures at 1 and 28 days, which has been reported in GGBS containing alkali activated systems [8, 47]. Hydrotalcite is found in all samples with different levels of GP replacement, indicating that its formation within this alkali activated system is dominated by GGBS with sufficient composition of Mg and Al. Quartz, mullite and

hematite peaks are identified as the remnant crystalline phases of incompletely reacted PCFA and their intensities change with different levels of GP replacement.

3.3.2 FTIR analysis

The FTIR spectra of paste mixture R, G10, G20 and G30 are shown in Figure 9. The overall broad band of interest is located between 800 and 1200 cm^{-1} as a result of phase overlapping from both precursors and reaction products. This band is widely accepted in the literature as the main T-O asymmetric stretching band and is used to study the changes of the amorphous gel structure (Ca/Si or Al/Si ratio) in AAMs [49, 50]. The main band in all spectra is centred at approximately 950 cm^{-1}, which is assigned to Si-O and/or Si-O-M bonds (M being alkali metal or alkali earth metal) [51]. More specifically, it could be associated with the Si-O-Si bonds of SiO_n units (n=2) [52], which is the representative structure of aluminosilicate chains containing C-A-S-H type gel formed in alkali activated GGBS.

From the analysis of the main T-O bands near 950 cm^{-1}, it can be observed that when the GP content increases, this band first shifts towards lower wavenumber from 1 day to 7 days but then it shifts to a higher wavenumber from 7 days to 28 days. This behavior can be associated with the type of vibrations: (i) the inner bond vibration inside T-O tetrahedral (T=Si or Al) and (ii) the vibration between T-O tetrahedral [53]. The lower force constant of Al compared with Si in the harmonious vibration model leads to lower vibration frequencies of Al-O bonds than Si-O bonds. Consequently, the observed main band shifts towards lower wavenumbers is due to the formation of the reaction products with an increased substitution of Si by Al [54, 55]. It is believed that Al dissolves more easily from the solid precursor structure due to the lower binding energy of Al-O compared with Si-O bonds. Therefore, the reaction products at 1 and

346 7 days curing have the tendency to form Al-rich structures [54, 56]. These findings are also in
347 line with previous studies on alkali activated fly ash [27]. At 28 days, the main band eventually
348 shifts to higher wavenumbers, indicating that more Si is incorporated into the gel network,
349 forming a more complete Si-rich structure. The phenomenon of main band movement to
350 higher wavenumber is also reported in cementitious systems as hydration proceeds and
351 indicates a higher polymerization degree and/or higher cross-linking of silica network in C-S-
352 H gel [57].
353 Furthermore, a more distinctive effect of the main band shifts can be observed in Figure 10.
354 A decline of the main band wavenumber at 1 and 7 days is found with higher GP replacements.
355 This effect can be associated with polymerization degree of the reaction products. Previous
356 studies on alkali activated GP observed sodium silicate gel formation within the system [18].
357 Higher GP replacement increases the amount of available silica at early ages, which have
358 major influence on the polymerization process. With higher silica concentration, soluble silica
359 in the pore solution at early ages is more likely to exist as monomer rather than highly
360 polymerized species [58]. Therefore, the initial average polymerization degree of the reaction
361 product is considerably lower. Accordingly, the main band is at lower wavenumber with higher
362 GP replacement at 1 and 7 days. On the other hand, the main band at 28 days with a higher
363 GP replacement shifts to higher wavenumber, which is in agreement with previous works
364 forming more Si rich and stable gel [54, 57, 59]. This also indicates a higher polymerization of
365 reaction products within the structure.

3.3.3 Paste heat evolution

Isothermal calorimetry is conducted on alkali activated pastes to evaluate their reaction kinetics and reaction degree. Heat flow curves of paste sample R, G10-G30 are shown in Figure 11(a). Two sub-calorimetric peaks are observed in all mixtures: The first peak is due to the wetting and dissolution of precursors particles and the second broader peak corresponds to the formation of reaction products. These results are in good agreement with those reported for silicate activated GGBS or GGBS/PCFA blends [15, 36, 60]. A decrease in the intensity of the second peak and a delay in its appearance is found with increasing GP. This longer induction period corresponds to a slow initial reaction kinetics because of dissolution of GP, after which the reactions finally accelerates when the ionic concentration reaches a critical threshold concentration [61]. The fast formation of initial reaction products around the unreacted GGBS or PCFA particles may account for this longer induction period. [62]. It is believed that the layer of reaction products thickens with increasing GP amount and prolongs the time required for available alkali and other useful species to penetrate through. Another reason is the higher amount of available silica species dissolved at initial stage, which increases the local activator modulus and eventually changes the local content of alkali activator. Previous studies by ^{29}Si NMR proved that higher amount of silica species with low polymerization degree (monomers) is achieved by lowering the activator modulus [63], which can speed up the gel formation. On the contrary, increased local activator modulus by GP replacement retards the reaction process and prolongs the induction period. Similar results have also been found in previous studies in activated GGBS/PCFA mixtures [15, 64].

387 The cumulative heat evolution of the paste mixtures is shown in Figure 11(b). A higher
388 cumulative heat is found with increasing GP content. It is well known that the total heat
389 release reflects the extent of reaction which may be correlated with enhanced compressive
390 strength development. The higher cumulative heat of activated GP compared to activated
391 PCFA (discussed in Section 3.1.4) can therefore be partly accounted for the observed higher
392 compressive strength (Figure 6) in these samples.
393 However, on the other hand, NaOH activated GP can produce soluble silica monomers that
394 are quite similar to the silica provided by water glass [19]. In fact, the calorimetric curves of
395 mixtures with increasing GP replacement share similar characteristics with those of alkali
396 activated GGBS/PCFA mixtures using NaOH and solid sodium silicate increasing silicate
397 modulus as activator [60]. Therefore, the higher cumulative heat release and the higher
398 compressive strength with increasing GP levels can also be partly due to the enhanced
399 reaction of GGBS by the more abundant released soluble silica.

400 ### 3.3.4 Thermogravimetric analysis

401 Differential thermogravimetric (DTG) curves of the paste mixtures (R and G10-G30) of 28 days
402 are presented in Figure 12(a). The major DTG peaks for all samples are between 105 to 300 ℃,
403 while the curves stabilize gradually after 500 ℃. The observed loss from 105 to 300 ℃ in DTG
404 curves represents decomposition of major reaction products. Such results are in good
405 agreement with previous literature reporting that the C-S-H type gel dehydration is found in
406 the temperature range of 180 to 300 ℃ in OPC systems [65] and of 105 to 300 ℃ in alkali
407 activated GGBS [15]. Additionally, the C-A-S-H type gel was reported to decompose between
408 105 and 300 ℃ [66]. Accordingly, these results may imply that C-A-S-H type gel is the dominant

409 reaction products in all investigated mixtures, which is responsible for the major mass loss.
410 The minor DTG peaks present at 300 to 400 °C in Figure 12(a) is attributed to the dehydration
411 and decarbonation of the present hydrotalcite [47], in line with existence of hydrotalcite
412 detected by XRD. Furthermore, very weak peaks are observed between 500 to 800 °C and
413 after 800 °C, mainly due to carbonated phases, decomposition and formation of new
414 crystalline phases.
415 It is assumed that the amount of main reaction products can be reflected by the percentage
416 of mass loss from 105 to 300 °C on the thermogravimetric (TG) curves in Figure 12(b). The
417 calculation is made with the assumption that the dominant reason for the mass loss within
418 105 to 300 °C is dehydration of C-A-S-H type gel. The sequence of mass loss is shown as
419 G30(6.36%)>G20(5.50%)>G10(4.33%)>R(4.16%), indicating that GP has significant effect on
420 the reaction process and largely facilitates the gel formation especially at higher replacement
421 levels. This result is in line with the data obtained from the calorimetry study which also
422 confirmed that the GP replacement enhances the total reaction degree of precursors and
423 leads to a higher cumulative heat production.

424 ### 3.3.5 ESEM/EDX analysis

425 Back Scattered electron (BSE) imaging was performed on all paste mixtures (R and G10-G30)
426 after 1, 7, and 28 days curing. Representative images of R and G30 mixtures are shown in
427 Figure 13. PCFA particles are light gray colored and generally have regular spherical shapes.
428 GP and GGBS particles are irregular polygonal shaped and are brighter due to the greater
429 amount of Ca. The gel phase generally shows a darker grey color with grey level lower than
430 PCFA, whereas pores filled with epoxy are black.

Comparison of the images of R and G30 pastes at the same curing time shows that G30 yields a denser and more homogenous microstructure at all ages, with more areas for gel phases and less pores. While paste R shows heterogeneously distributed pores, indicating a more porous matrix. These results are in good agreement with those deduced from the thermogravimetry and isothermal calorimetry, which again qualitatively prove that increasing GP enhances the gel formation.

In order to get additional information about the reaction products, EDX analysis of multiple randomly-selected points within the binder region (excluding unreacted particles) was carried out on R and G30 at 1, 7, and 28 days. Calcium, aluminum and silicon are normalized to 100% on an oxide basis and plotted in the CaO-SiO_2-Al_2O_3 ternary diagram in Figure 14, which can reflect the nature of the reaction products in R and G30. It can be observed that for both R and G30 the experimental data fall in the region of alkali activated slag [42, 47, 67] as well as GGBS/PCFA systems [8, 10, 12, 15, 68-70]. Considering the poorly crystalline C-S-H phase presence detected by the XRD and typical chemical bonds identified by FTIR analysis, the main reaction products are assumed to be C-S-H gel dominant. In addition, Al incorporation into the structure is identified by EDX indicating formation of a C-A-S-H type gel. Presences of Na in the reaction products are also confirmed by EDX analysis on R and G30 mixture at 28 days, which suggests the existence other analogous gel types. For instance, N-A-S-H type gel intermixing with C-A-S-H type gel or C-(N)-A-S-H type gel (sodium incorporated C-A-S-H gel), in which Na cations serve as negative charge balance in the structure. N-A-S-H type gel is widely accepted as a 3-dimensional aluminosilicate network existing in activated PCFA [9, 27, 71] or activated GGBS/PCFA binders with a dominant fly ash content [10, 15]. Its gel structure

453 is commonly accepted to be “zeolite” related and is strongly correlated with the formation of
454 crystalline zeolite within the system [22, 72]. In this study, the XRD patterns of all the paste
455 mixtures up to 28 days did not give any evidence of zeolite phases. Furthermore, FTIR revealed
456 no absorption band inside the main T-O band for N-A-S-H type gel. All these evidences imply
457 that N-A-S-H gel was not formed in the structure and the main reaction product in all alkali-
458 activated binders is a C-(N)-A-S-H type gel.
459

4 Conclusions

This paper investigated the reactivity and potential of waste glass as partial replacement for PCFA in alkali activated GGBS/PCFA systems. The precursors were systematically characterized followed by a detailed microstructural analysis of the paste mixtures as well as the reaction kinetics. The following conclusions can be drawn from this research:

- Waste glass powder exhibits high reactivity for alkaline activation under room temperature compared with PCFA, which is due to its finer particle size, higher specific area, high amorphous phases contents and high reactive phases content (Si, Ca).
- The compressive strength increased by 35% with increasing GP (as a PCFA replacement) up to 30% in the GGBS-PCFA-GP system. These results along with thermogravimetry and calorimetry analysis confirm that the GP is actively involved in the reaction process.
- GP as PCFA replacement contributes to more available silica and Ca dissolution and largely facilitates the gel formation. A higher polymerization of the gel network is also observed.
- The compressive strength increment, the enhanced gel formation and the prolonged induction period are similar with the conjugational effect of using both sodium hydroxide and sodium silicate alkali activator in alkali-activated slag/fly ash system.
- The microstructural analysis shows that the dominant reaction product is a C-(N)-A-S-H type gel. No N-A-S-H type gel is formed in the system.
- The feasibility of potential use of waste glass as binder precursor for production of AAMs was confirmed. This can offer a solution for both alkaline cement industry to provide a new precursor and glass industry to solve the storage issue and their related economic

cost and environmental impact.

Acknowledgement

This research is supported by Van Gansewinkel Minerals and Microlab, Section Materials and Environment, Faculty of Civil Engineering and Geosciences, Delft University of Technology. The authors gratefully acknowledge Van Gansewinkel Maltha for supplying the GP fraction and additional data. In addition, the authors would like to thank Mr. Y. Zuo for the discussion on FTIR analysis and Dr. B. Ghiassi for the assistance on manuscript improvement.

Reference

[1] The European Container Glass Federation, Glass packaging closed loop recycling up to 74% in the EU. http://feve.org/about-glass/statistics/, 2016.

[2] A. Keulen, Report on waste minerals and solutions: Waste minerals SEMBRES project, Van Gansewinkel Minerals, 2013.

[3] L.M. Federico, S.E. Chidiac, Waste glass as a supplementary cementitious material in concrete – Critical review of treatment methods, Cement and Concrete Composites, 31 (2009) 606-610.

[4] C. Shi, K. Zheng, A review on the use of waste glasses in the production of cement and concrete, Resources, Conservation and Recycling, 52 (2007) 234-247.

[5] Y. Jani, W. Hogland, Waste glass in the production of cement and concrete – A review, Journal of Environmental Chemical Engineering, 2 (2014) 1767-1775.

[6] P. Duxson, J.L. Provis, G.C. Lukey, J.S. Van Deventer, The role of inorganic polymer technology in the development of 'green concrete', Cement and Concrete Research, 37 (2007) 1590-1597.

[7] A. Buchwald, M. Schulz, Alkali-activated binders by use of industrial by-products, Cement and Concrete Research, 35 (2005) 968-973.

[8] F. Puertas, A. Fernández-Jiménez, Mineralogical and microstructural characterisation of alkali-activated fly ash/slag pastes, Cement and Concrete composites, 25 (2003) 287-292.

[9] A. Palomo, M. Grutzeck, M. Blanco, Alkali-activated fly ashes: a cement for the future, Cement and Concrete Research, 29 (1999) 1323-1329.

[10] I. Ismail, S.A. Bernal, J.L. Provis, R. San Nicolas, S. Hamdan, J.S. van Deventer, Modification of phase evolution in alkali-activated blast furnace slag by the incorporation of fly ash, Cement and Concrete Composites, 45 (2014) 125-135.

[11] S. Kumar, R. Kumar, S. Mehrotra, Influence of granulated blast furnace slag on the reaction, structure and properties of fly ash based geopolymer, Journal of materials science, 45 (2010) 607-615.

[12] F. Puertas, S. Martı´nez-Ramı´rez, S. Alonso, T. Vazquez, Alkali-activated fly ash/slag cements: strength behaviour and hydration products, Cement and Concrete Research, 30 (2000) 1625-1632.

[13] K. Arbi, M. Nedeljkovic, Y. Zuo, G. Ye, A Review on the Durability of Alkali-Activated Fly Ash/Slag Systems: Advances, Issues, and Perspectives, Industrial & Engineering Chemistry Research, 55 (2016) 5439-5453.

[14] S. Puligilla, P. Mondal, Co-existence of aluminosilicate and calcium silicate gel characterized through selective dissolution and FTIR spectral subtraction, Cement and Concrete Research, 70 (2015) 39-49.

[15] X. Gao, Q.L. Yu, H.J.H. Brouwers, Reaction kinetics, gel character and strength of ambient temperature cured alkali activated slag–fly ash blends, Construction and Building Materials, 80 (2015) 105-115.

[16] M. Tashima, L. Soriano, M. Borrachero, J. Monzó, C. Cheeseman, J. Payá, Alkali activation of vitreous calcium aluminosilicate derived from glass fiber waste, Journal of Sustainable Cement-Based Materials, 1 (2012) 83-93.

[17] M.T.T. Ana Balaguer Pascual, Arezki Tagnit-Hamou, Waste glass powder-based alkali-activated mortar, NTCC2014: International Conference on Non-Traditional Cement and Concrete, 2014.
[18] R. Redden, N. Neithalath, Microstructure, strength, and moisture stability of alkali activated glass powder-based binders, Cement and Concrete Composites, 45 (2014) 46-56.
[19] M. Torres-Carrasco, J. Palomo, F. Puertas, Sodium silicate solutions from dissolution of glasswastes. Statistical analysis, Materiales de Construcción, 64 (2014) e014.
[20] F. Puertas, M. Torres-Carrasco, Use of glass waste as an activator in the preparation of alkali-activated slag. Mechanical strength and paste characterisation, Cement and Concrete Research, 57 (2014) 95-104.
[21] J.L. Provis, J.S. van Deventer, Alkali Activated Materials: State-of-the-art Report, RILEM TC 224-AAM, Springer Dordrecht2014.
[22] J.L. Provis, J.S.J. Van Deventer, Geopolymers: structures, processing, properties and industrial applications, Elsevier2009.
[23] A. Fernández-Jiménez, F. Puertas, Effect of activator mix on the hydration and strength behaviour of alkali-activated slag cements, Advances in cement research, 15 (2003) 129-136.
[24] S. Song, H.M. Jennings, Pore solution chemistry of alkali-activated ground granulated blast-furnace slag, Cement and Concrete Research, 29 (1999) 159-170.
[25] NEN, 7341. Leaching characteristics of solid earhty and stony building and waste materials - Determination of the availability of inorganic components for leaching, 1994.
[26] A. Fernández-Jimenez, A. De La Torre, A. Palomo, G. López-Olmo, M. Alonso, M. Aranda, Quantitative determination of phases in the alkali activation of fly ash. Part I. Potential ash reactivity, Fuel, 85 (2006) 625-634.
[27] Y. Ma, Microstructure and Engineering Properties of Alkali Activated Fly Ash, (2013).
[28] NEN, 196-1. Methods of testing cement–Part 1: Determination of strength, European Committee for standardization, (2005).
[29] W. Lee, J. Van Deventer, Structural reorganisation of class F fly ash in alkaline silicate solutions, Colloids and Surfaces A: Physicochemical and Engineering Aspects, 211 (2002) 49-66.
[30] A. Hajimohammadi, J.L. Provis, J.S.J. van Deventer, The effect of silica availability on the mechanism of geopolymerisation, Cement and Concrete Research, 41 (2011) 210-216.
[31] S.S. Kouassi, J. Andji, J.-P. Bonnet, S. Rossignol, Dissolution of waste glasses in high alkaline solutions, Ceramics-Silikáty, 54 (2010) 235-240.
[32] E.H. Oelkers, S.R. Gislason, The mechanism, rates and consequences of basaltic glass dissolution: I. An experimental study of the dissolution rates of basaltic glass as a function of aqueous Al, Si and oxalic acid concentration at 25 C and pH= 3 and 11, Geochimica et Cosmochimica Acta, 65 (2001) 3671-3681.

[33] P. Duxson, J.L. Provis, Designing precursors for geopolymer cements, Journal of the American Ceramic Society, 91 (2008) 3864-3869.
[34] C.K. Yip, G.C. Lukey, J.L. Provis, J.S.J. van Deventer, Effect of calcium silicate sources on geopolymerisation, Cement and Concrete Research, 38 (2008) 554-564.
[35] K. Newlands, The early stage dissolution characteristics of aluminosilicate glasses, University of Aberdeen, 2015.
[36] S. Chithiraputhiran, N. Neithalath, Isothermal reaction kinetics and temperature dependence of alkali activation of slag, fly ash and their blends, Construction and Building Materials, 45 (2013) 233-242.
[37] D.P. Tuchman, Research toward direct analysis of quartz dust on filters using FTIR spectroscopy, US Department of the Interior, Bureau of Mines1992.
[38] F.B. Reig, J.G. Adelantado, M.M. Moreno, FTIR quantitative analysis of calcium carbonate (calcite) and silica (quartz) mixtures using the constant ratio method. Application to geological samples, Talanta, 58 (2002) 811-821.
[39] W. Taylor, Application of infrared spectroscopy to studies of silicate glass structure: Examples from the melilite glasses and the systems Na2O-SiO2 and Na2O-Al2O3-SiO2, Proceedings of the Indian Academy of Sciences-Earth and Planetary Sciences, 99 (1990) 99-117.
[40] Z. Zhang, H. Wang, J.L. Provis, Quantitative study of the reactivity of fly ash in geopolymerization by FTIR, Journal of Sustainable Cement-Based Materials, 1 (2012) 154-166.
[41] S.L. Valcke, P. Pipilikaki, H.R. Fischer, M.H. Verkuijlen, E.R. van Eck, FT-IR and 29Si-NMR for evaluating aluminium–silicate precursors for geopolymers, Materials and Structures, (2014) 1-13.
[42] D. Ravikumar, N. Neithalath, Effects of activator characteristics on the reaction product formation in slag binders activated using alkali silicate powder and NaOH, Cement and Concrete Composites, 34 (2012) 809-818.
[43] B.G. Kutchko, A.G. Kim, Fly ash characterization by SEM–EDS, Fuel, 85 (2006) 2537-2544.
[44] M. Dudas, C. Warren, Submicroscopic model of fly ash particles, Geoderma, 40 (1987) 101-114.
[45] Z. Yu, Microstructure Development and Transport Properties of Portland Cement-fly Ash Binary Systems: in view of service life predictions, TU Delft, Delft University of Technology, 2015.
[46] N. Peronius, T. Sweeting, On the correlation of minimum porosity with particle size distribution, Powder technology, 42 (1985) 113-121.
[47] S.-D. Wang, K.L. Scrivener, Hydration products of alkali activated slag cement, Cement and Concrete Research, 25 (1995) 561-571.
[48] J.I. Escalante‐García, A.F. Fuentes, A. Gorokhovsky, P.E. Fraire‐Luna, G. Mendoza‐Suarez, Hydration Products and Reactivity of Blast‐Furnace Slag Activated by Various Alkalis, Journal of the American Ceramic Society, 86 (2003) 2148-2153.

[49] M. Criado, A. Fernández-Jiménez, A. Palomo, Alkali activation of fly ash: Effect of SiO_2/Na_2O ratio: Part I: FTIR study, Microporous and mesoporous materials, 106 (2007) 180-191.
[50] C.A. Rees, J.L. Provis, G.C. Lukey, J.S. van Deventer, Attenuated total reflectance fourier transform infrared analysis of fly ash geopolymer gel aging, Langmuir, 23 (2007) 8170-8179.
[51] W. Lee, J. Van Deventer, Use of infrared spectroscopy to study geopolymerization of heterogeneous amorphous aluminosilicates, Langmuir, 19 (2003) 8726-8734.
[52] N. Clayden, S. Esposito, A. Aronne, P. Pernice, Solid state 27 Al NMR and FTIR study of lanthanum aluminosilicate glasses, Journal of non-crystalline solids, 258 (1999) 11-19.
[53] J.A. Gadsden, Infrared Spectra of Minerals and Related Inorganic Compounds, Butterworths1975.
[54] A. Fernández-Jiménez, A. Palomo, Mid-infrared spectroscopic studies of alkali-activated fly ash structure, Microporous and Mesoporous Materials, 86 (2005) 207-214.
[55] A. Fernández-Jiménez, A.G. de la Torre, A. Palomo, G. López-Olmo, M.M. Alonso, M.A.G. Aranda, Quantitative determination of phases in the alkaline activation of fly ash. Part II: Degree of reaction, Fuel, 85 (2006) 1960-1969.
[56] P. Duxson, A. Fernández-Jiménez, J. Provis, G. Lukey, A. Palomo, J. Van Deventer, Geopolymer technology: the current state of the art, Journal of Materials Science, 42 (2007) 2917-2933.
[57] I. Garcia-Lodeiro, A. Fernández-Jiménez, D. Macphee, I. Sobrados, J. Sanz, A. Palomo, Stability of synthetic calcium silicate hydrate gels in presence of alkalis, aluminum, and soluble silica, Transportation Research Record: Journal of the Transportation Research Board, (2010) 52-57.
[58] J.L. Provis, P. Duxson, G.C. Lukey, F. Separovic, W.M. Kriven, J.S. van Deventer, Modeling speciation in highly concentrated alkaline silicate solutions, Industrial & engineering chemistry research, 44 (2005) 8899-8908.
[59] C.A. Rees, J.L. Provis, G.C. Lukey, J.S. van Deventer, In situ ATR-FTIR study of the early stages of fly ash geopolymer gel formation, Langmuir, 23 (2007) 9076-9082.
[60] D. Ravikumar, N. Neithalath, Reaction kinetics in sodium silicate powder and liquid activated slag binders evaluated using isothermal calorimetry, Thermochimica Acta, 546 (2012) 32-43.
[61] J. Provis, J. Van Deventer, Geopolymerisation kinetics. 2. Reaction kinetic modelling, Chemical Engineering Science, 62 (2007) 2318-2329.
[62] J.D. Rimer, R.F. Lobo, D.G. Vlachos, Physical basis for the formation and stability of silica nanoparticles in basic solutions of monovalent cations, Langmuir, 21 (2005) 8960-8971.
[63] M. Criado, A. Fernández-Jiménez, A. Palomo, I. Sobrados, J. Sanz, Effect of the SiO_2/Na_2O ratio on the alkali activation of fly ash. Part II: ^{29}Si MAS-NMR Survey, Microporous and Mesoporous Materials, 109 (2008) 525-534.

[64] A. Brough, M. Holloway, J. Sykes, A. Atkinson, Sodium silicate-based alkali-activated slag mortars: Part II. The retarding effect of additions of sodium chloride or malic acid, Cement and Concrete Research, 30 (2000) 1375-1379.
[65] L. Alarcon-Ruiz, G. Platret, E. Massieu, A. Ehrlacher, The use of thermal analysis in assessing the effect of temperature on a cement paste, Cement and Concrete research, 35 (2005) 609-613.
[66] M.J. DeJong, F.-J. Ulm, The nanogranular behavior of CSH at elevated temperatures (up to 700 C), Cement and Concrete Research, 37 (2007) 1-12.
[67] I. Richardson, A. Brough, G. Groves, C. Dobson, The characterization of hardened alkali-activated blast-furnace slag pastes and the nature of the calcium silicate hydrate (CSH) phase, Cement and Concrete Research, 24 (1994) 813-829.
[68] N.K. Lee, H.K. Lee, Reactivity and reaction products of alkali-activated, fly ash/slag paste, Construction and Building Materials, 81 (2015) 303-312.
[69] E. Deir, B.S. Gebregziabiher, S. Peethamparan, Influence of starting material on the early age hydration kinetics, microstructure and composition of binding gel in alkali activated binder systems, Cement and Concrete Composites, 48 (2014) 108-117.
[70] F. Puertas, M. Palacios, H. Manzano, J.S. Dolado, A. Rico, J. Rodríguez, A model for the C-A-S-H gel formed in alkali-activated slag cements, Journal of the European Ceramic Society, 31 (2011) 2043-2056.
[71] A. Fernández-Jiménez, A. Palomo, M. Criado, Microstructure development of alkali-activated fly ash cement: a descriptive model, Cement and Concrete Research, 35 (2005) 1204-1209.
[72] S. Alonso, A. Palomo, Alkaline activation of metakaolin and calcium hydroxide mixtures: influence of temperature, activator concentration and solids ratio, Materials Letters, 47 (2001) 55-62.

Tables list

Table 1: Chemical composition of solid precursors by XRF.

Table 2: Paste mixture designs.

Table 3: Insoluble residue (I.R.) chemical composition of GP and PCFA by XRF.

Table 4: Amorphous phase and reactive element content (wt.%) in GP and PCFA.

Figures list

Figure 1: Particle size distribution of GP, PCFA and GGBS.

Figure 2: XRD patterns of unreacted solid precursors.

Figure 3: Element dissolution in time of Si (a), Al (b) and Ca (c) for PCFA and GP.

Figure 4: (a) heat flow and (b) cumulative heat evolution of alkali activated precursor (L/S=0.6).

Figure 5: FTIR spectra of original, residue and dissolved phases in (a) GP and (b) PCFA.

Figure 6: Compressive strength development of paste mixtures with increasing GP as PCFA replacement.

Figure 7: Pore structure of original PCFA and 4M NaOH-treated PCFA: (a) cumulative pore size distribution and (b) differential pore size distribution.

Figure 8: XRD pattern of GGBS/PCFA pastes with various amounts of GP as PCFA replacement at (a) 1 day and (b) 28 days, (C-S-H= Calcium Silicate Hydrate; Q= Quartz; M= Mullite; C=Calcite; Ht= Hydrotalcite).

Figure 9: FTIR spectra of pastes mixtures (a) R, (b) G10, (c) G20 and (d) G30 at 1, 7, and 28 days.

Figure 10: Change in wavenumber of the main T-O band for paste samples as a function of curing time and GP as PCFA replacement.

709 Figure 11: (a) Heat flow rate and (b) cumulative heat evolution of alkali activated paste
710 mixtures (L/S ratio 0.42).
711 Figure 12: (a) Differential thermogravimetry (DTG) curves and (b) thermogravimetry (TG)
712 curves of alkali activated paste mixtures.
713 Figure 13: BSE images of paste mixtures R and G30 cured for 1, 7 and 28 days.
714 Figure 14: Representative ternary diagram of EDX spot analysis for (a) R and (b) G30 mixtures
715 cured for 1,7, and 28 days.

716 **Tables**

717

718 Table 1: Chemical composition of solid precursors by XRF.

Oxide (wt. %)	SiO_2	Al_2O_3	Fe_2O_3	CaO	MgO	SO_3	Na_2O	K_2O	LOI_{950}
GP	65.60	2.37	2.40	22.06	2.17	0.39	1.99	0.86	2.00
PCFA	52.90	26.96	6.60	4.36	1.50	0.73	0.17	-	3.37
GGBS	32.91	11.84	0.46	40.96	9.23	1.60	-	0.33	1.15

719

720

721 Table 2: Paste mixture designs

Sample	L/S ratio	Activator	GGBS (wt. %)	PCFA (wt. %)	GP (wt. %)
R	0.42	4M NaOH Solution	50	50	0
G10				40	10
G20				30	20
G30				20	30

722

723

724 Table 3: Insoluble residue (I.R.) chemical composition of GP and PCFA by XRF

Oxide (wt. %)	SiO_2	Al_2O_3	Fe_2O_3	CaO	MgO	SO_3	Na_2O	K_2O	TiO_2
GP	62.24	7.96	0.77	18.01	3.86	0.16	0.59	3.29	1.82
PCFA	43.59	50.59	3.18	0.189	-	0.12	-	0.69	1.46

725

726

727 Table 4: Amorphous phase and reactive element content (wt.%) in GP and PCFA

Precursor	I.R.	Amorphous content	Total SiO_2	Reactive SiO_2	Total Al_2O_3	Reactive Al_2O_3	Total CaO
GP	18.14	81.86	65.60	54.31	2.37	0.92	22.06
PCFA	22.63	77.37	52.90	43.04	26.96	15.51	0.19

728

729 **Figures**

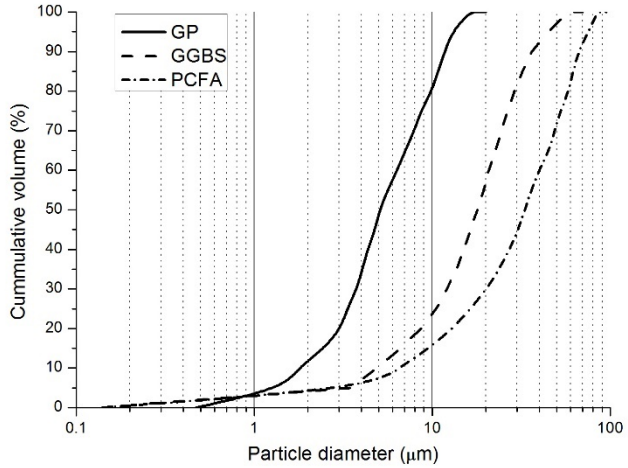

730

731 **Figure 1: Particle size distribution of GP, PCFA and GGBS.**

732

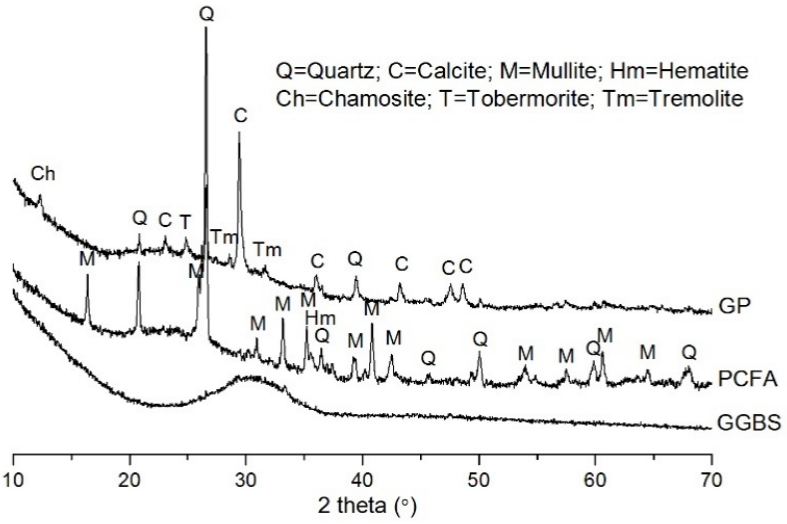

733

734 **Figure 2: XRD patterns of unreacted solid precursors**

735

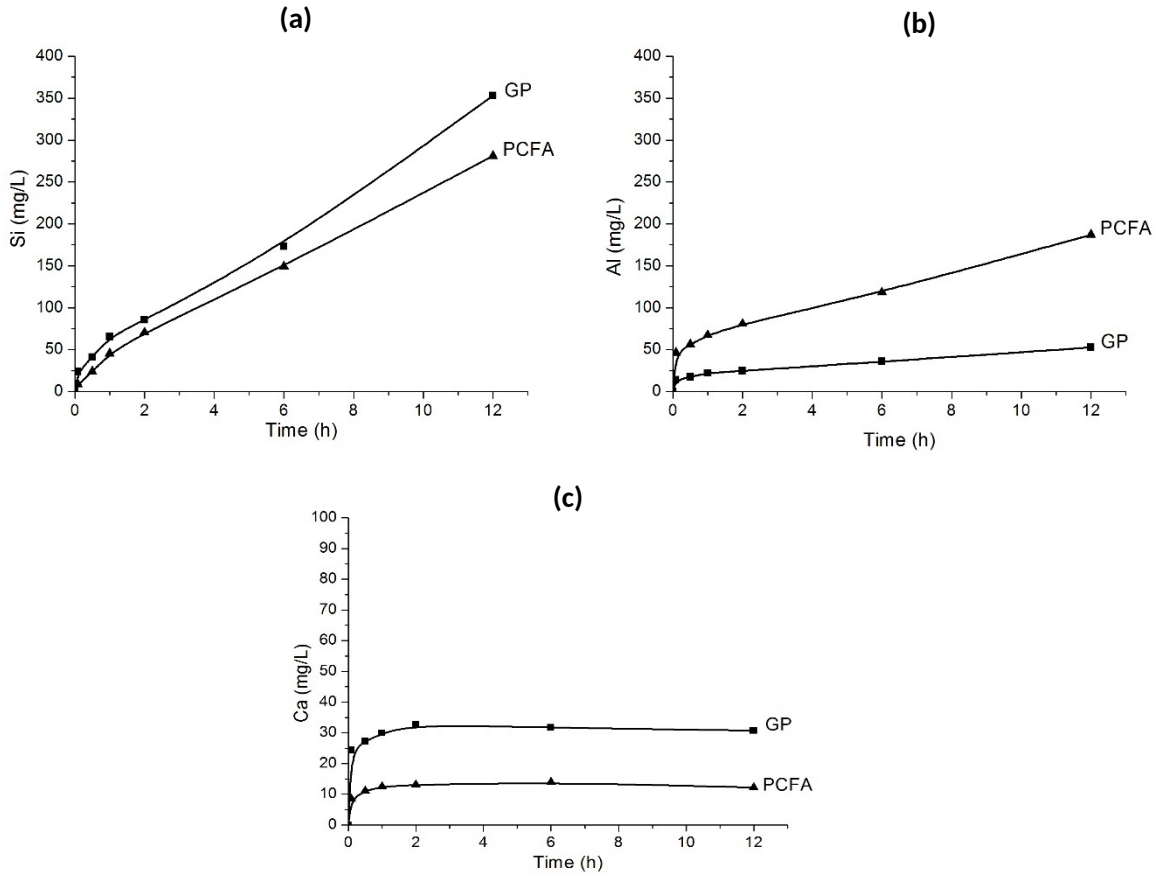

736

737 **Figure 3: Element dissolution in time of Si (a), Al (b) and Ca (c) for PCFA and GP.**

738

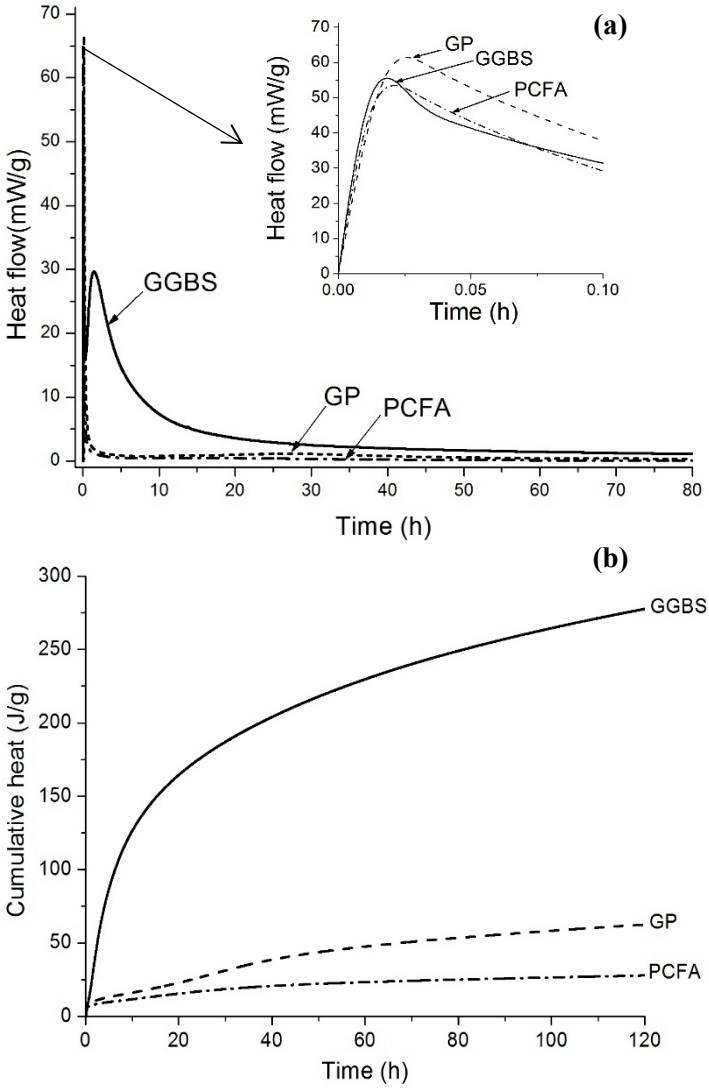

739

740 **Figure 4: (a) heat flow and (b) cumulative heat evolution of alkali activated precursor**

741 **(L/S=0.6).**

742

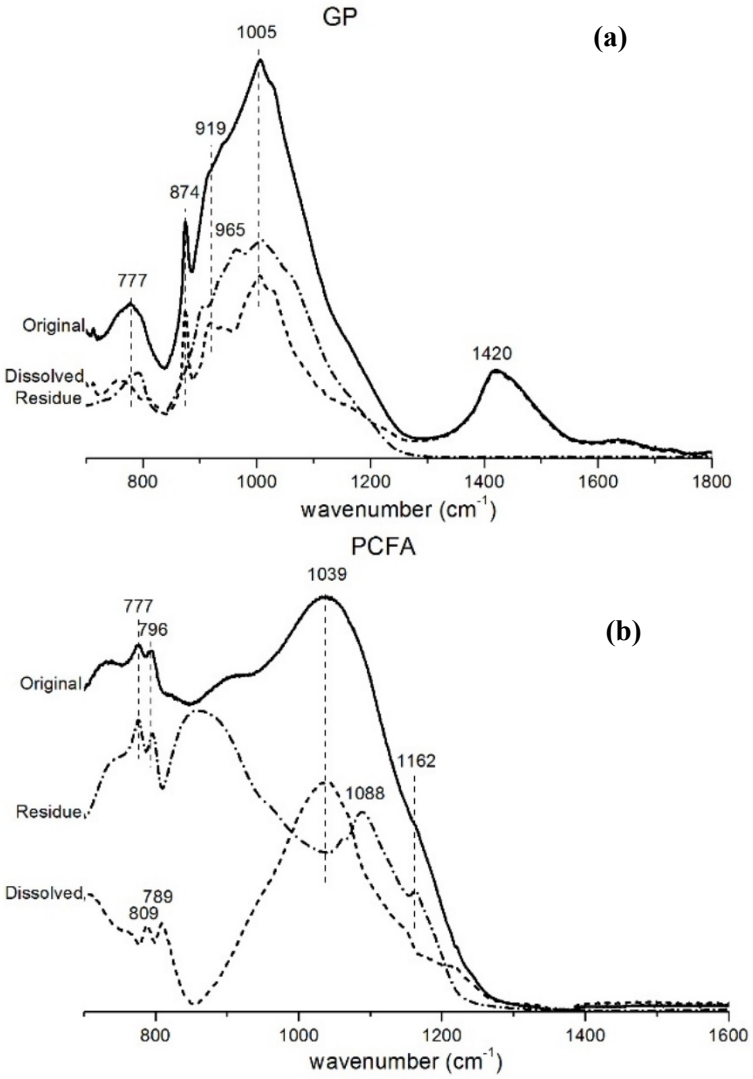

743

744 **Figure 5: FTIR spectra of original, residue and dissolved phases in (a) GP and (b) PCFA.**

745

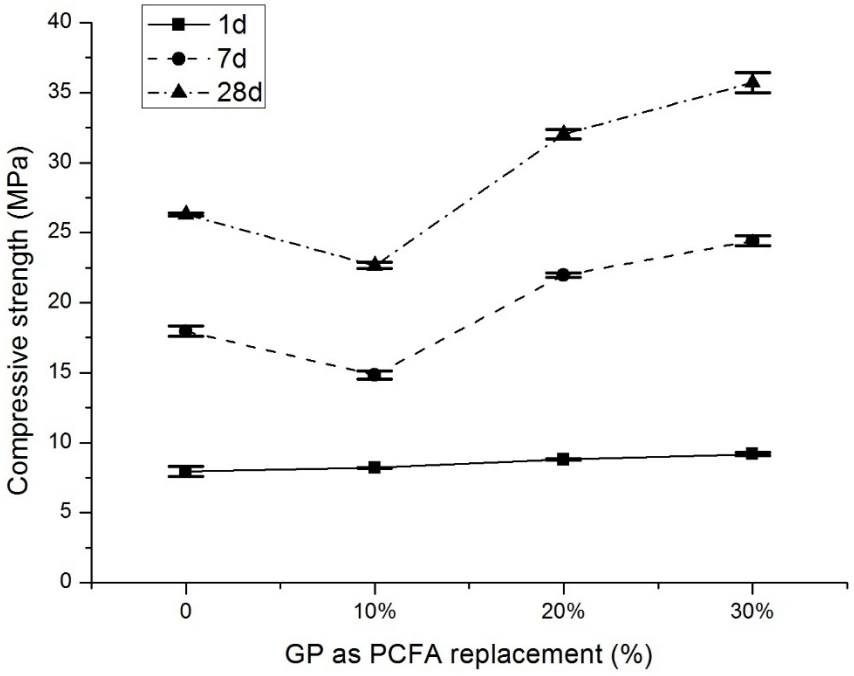

746

747 **Figure 6: Compressive strength development of paste mixtures with increasing GP as PCFA**

748 **replacement.**

749

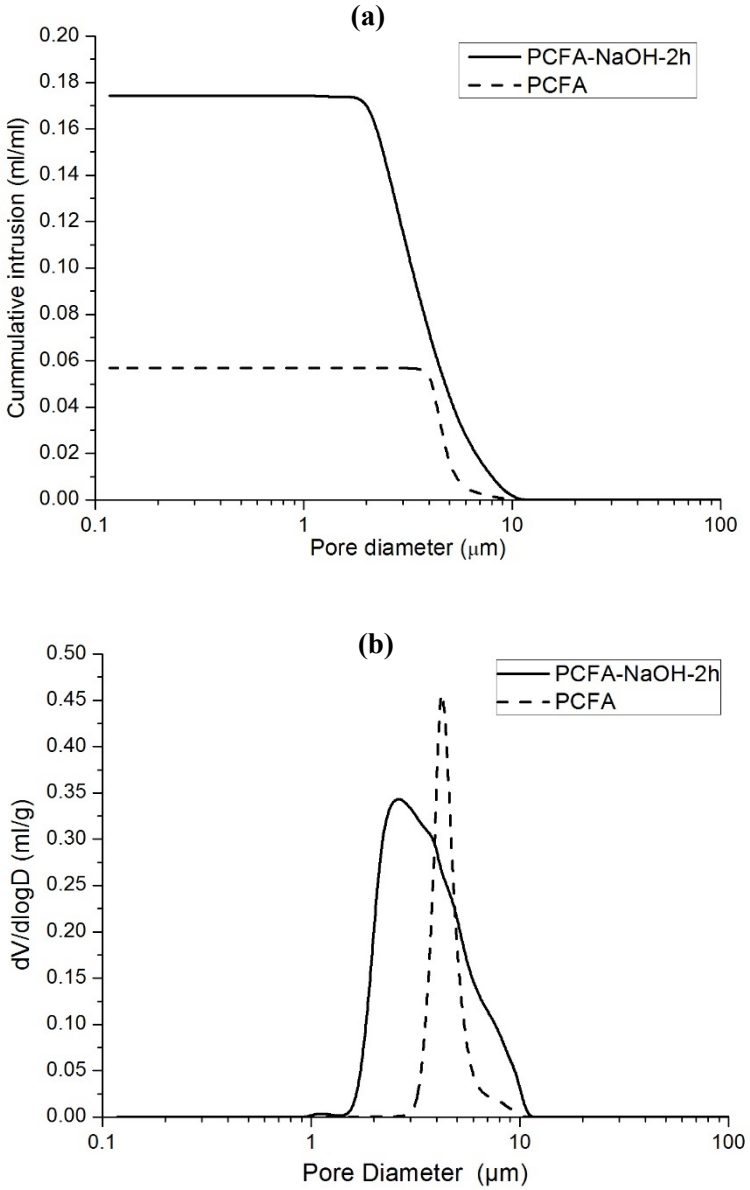

750

751 **Figure 7: Pore structure of original PCFA and 4M NaOH-treated PCFA: (a) cumulative pore**

752 **size distribution and (b) differential pore size distribution.**

753

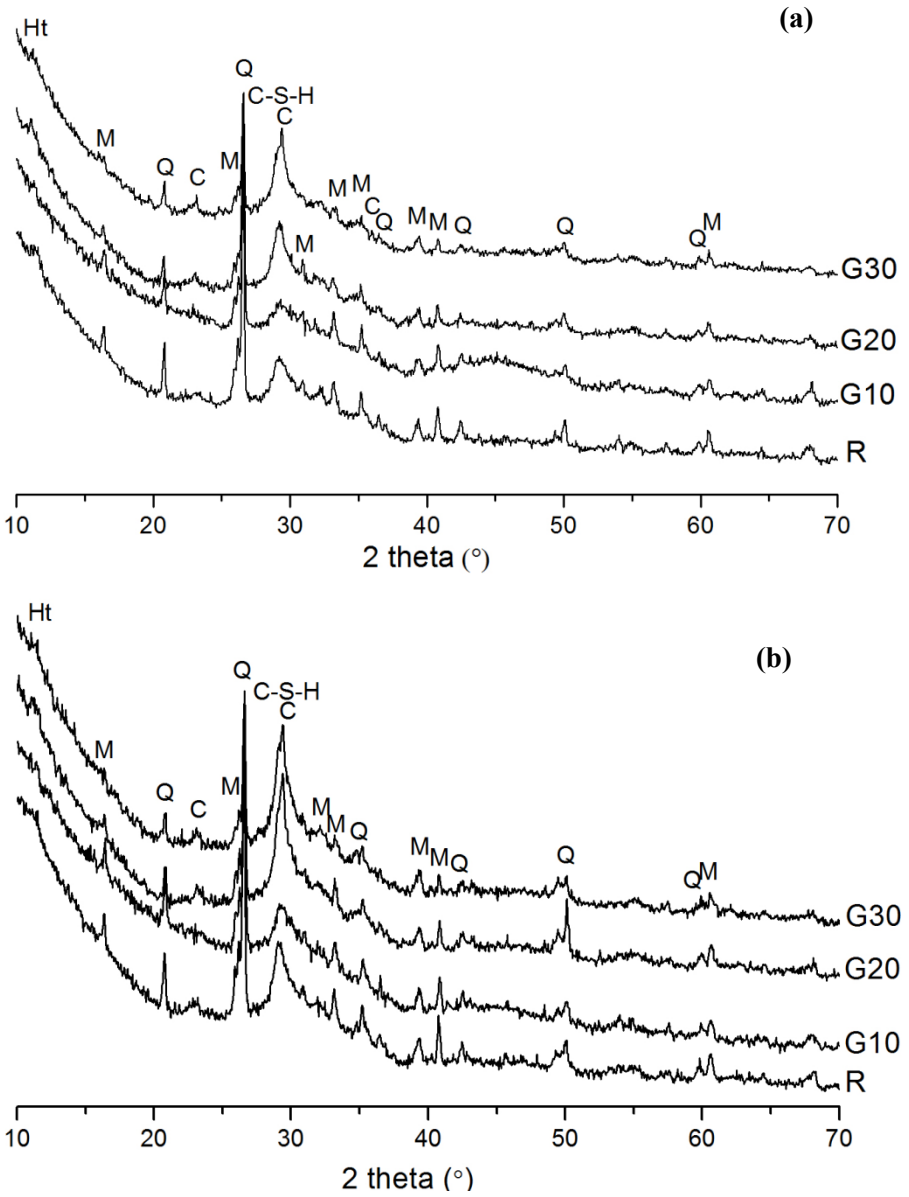

754

755 **Figure 8: XRD pattern of GGBS/PCFA pastes with various amounts of GP as PCFA**

756 **replacement at (a) 1 day and (b) 28 days, (C-S-H=Calcium Silicate Hydrate; Q=Quartz;**

757 **M=Mullite; C=Calcite; Ht=Hydrotalcite).**

758

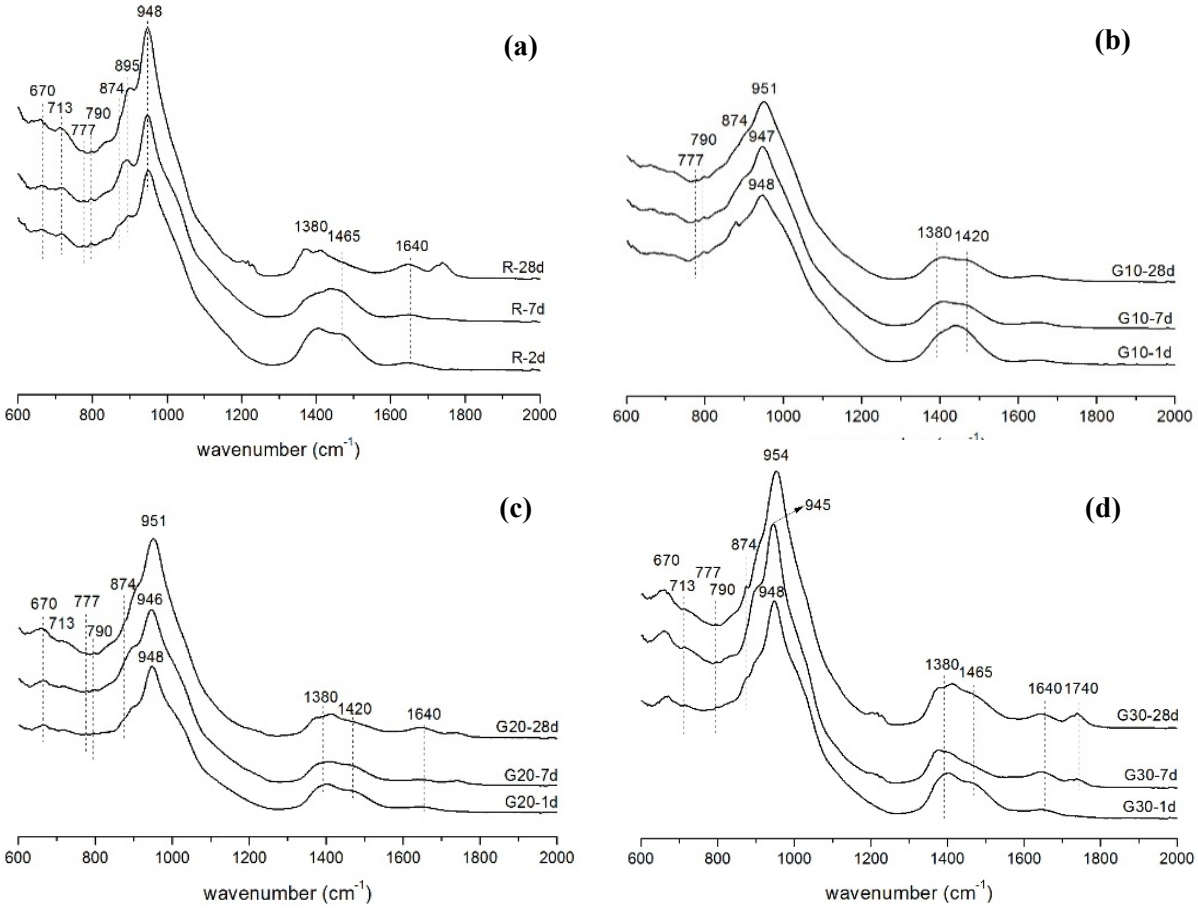

759

760 **Figure 9: FTIR spectra of pastes mixtures (a) R, (b) G10, (c) G20 and (d) G30 at 1, 7, and 28**

761 **days.**

762

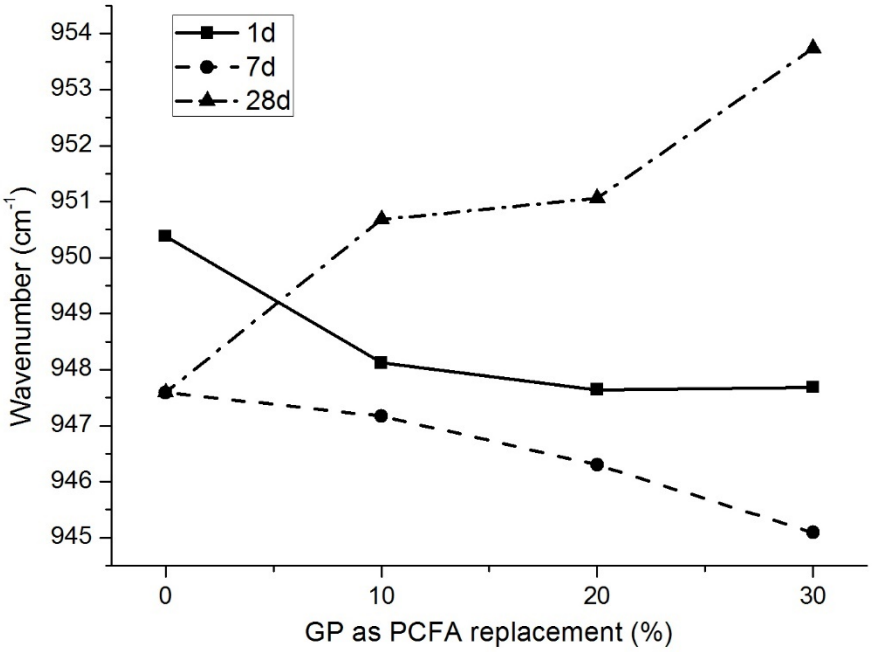

763

764 **Figure 10: Changes in wavenumber of the main T-O band for paste mixtures as a function of**

765 **curing time and GP as PCFA replacement.**

766

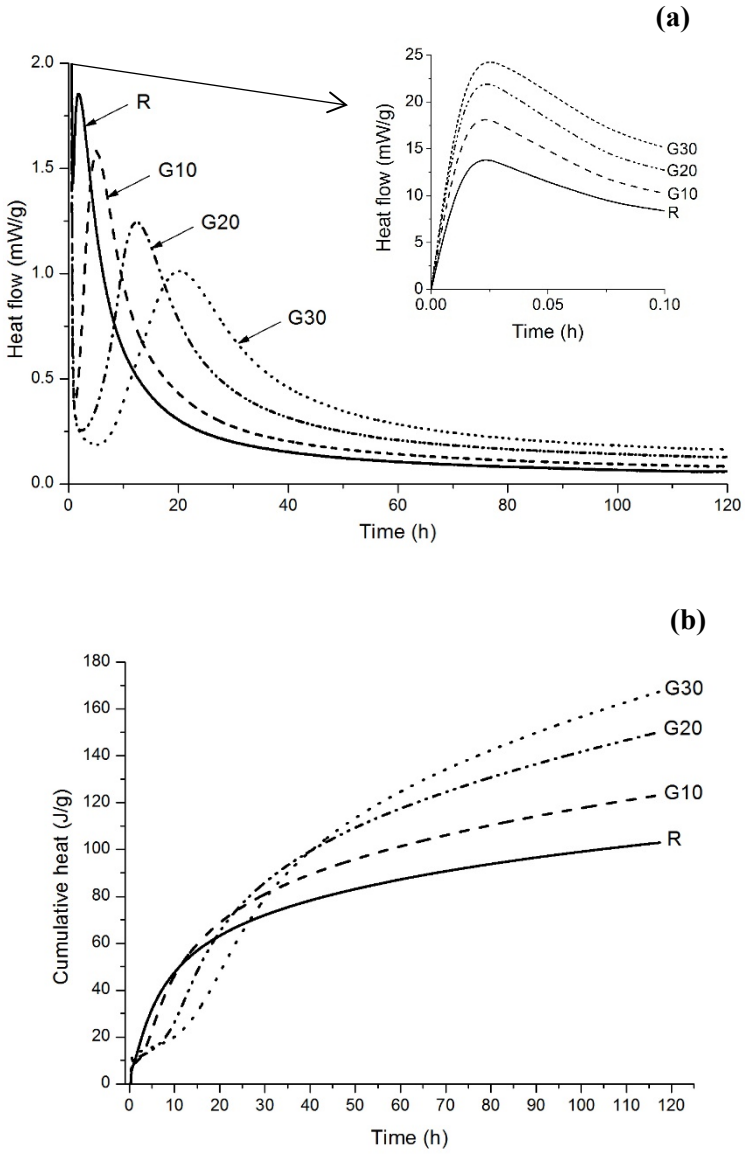

767

768 **Figure 11: (a) Heat flow rate and (b) cumulative heat evolution of alkali activated paste**

769 **mixtures (L/S ratio 0.42).**

770

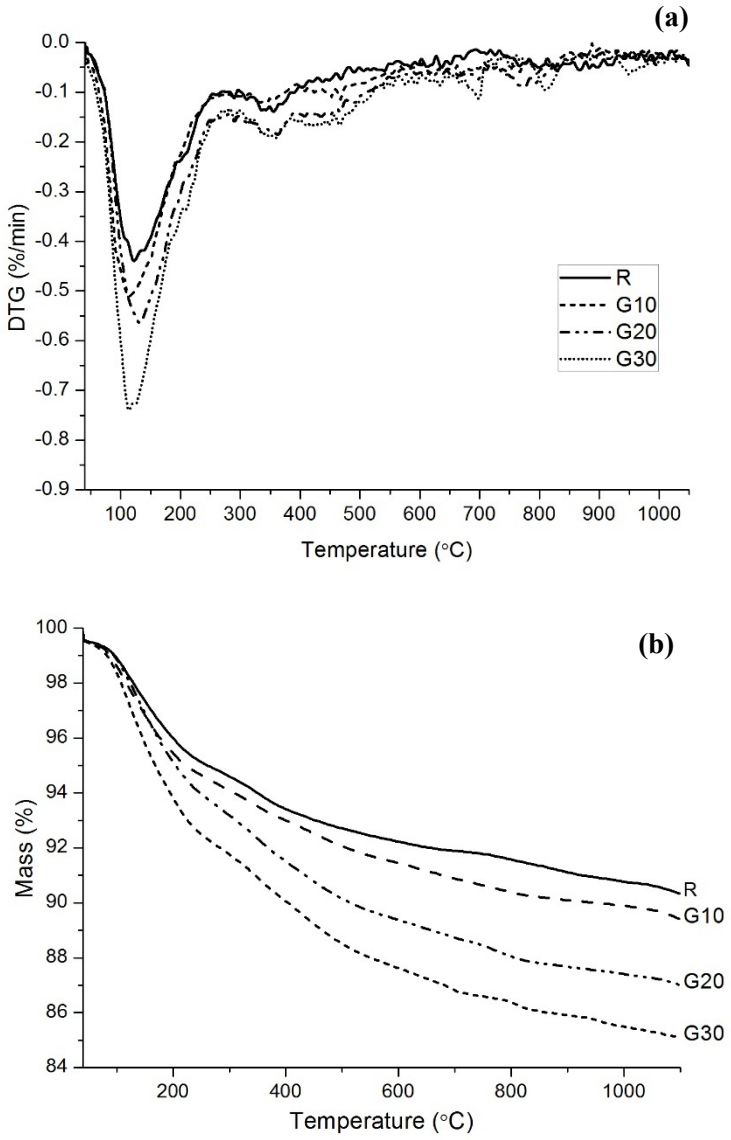

771

772 **Figure 12: (a) Differential thermogravimetry (DTG) and (b) thermogravimetry (TG) curves of**

773 **alkali activated paste mixtures.**

774

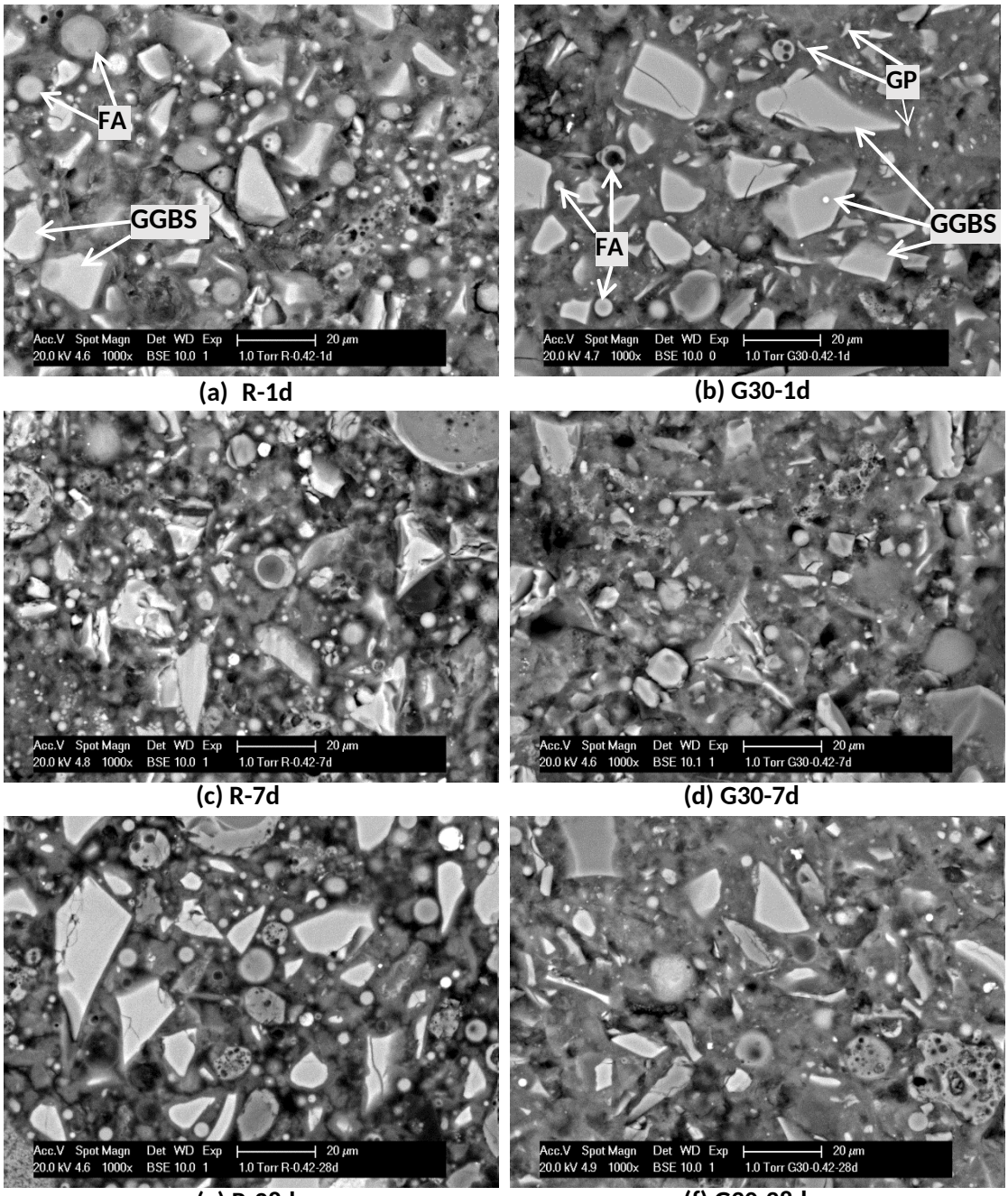

(a) R-1d **(b) G30-1d**

(c) R-7d **(d) G30-7d**

(e) R-28d **(f) G30-28d**

775

776 **Figure 13: Representative BSE images of paste mixture R and G30 cured for 1, 7 and 28 days.**

777

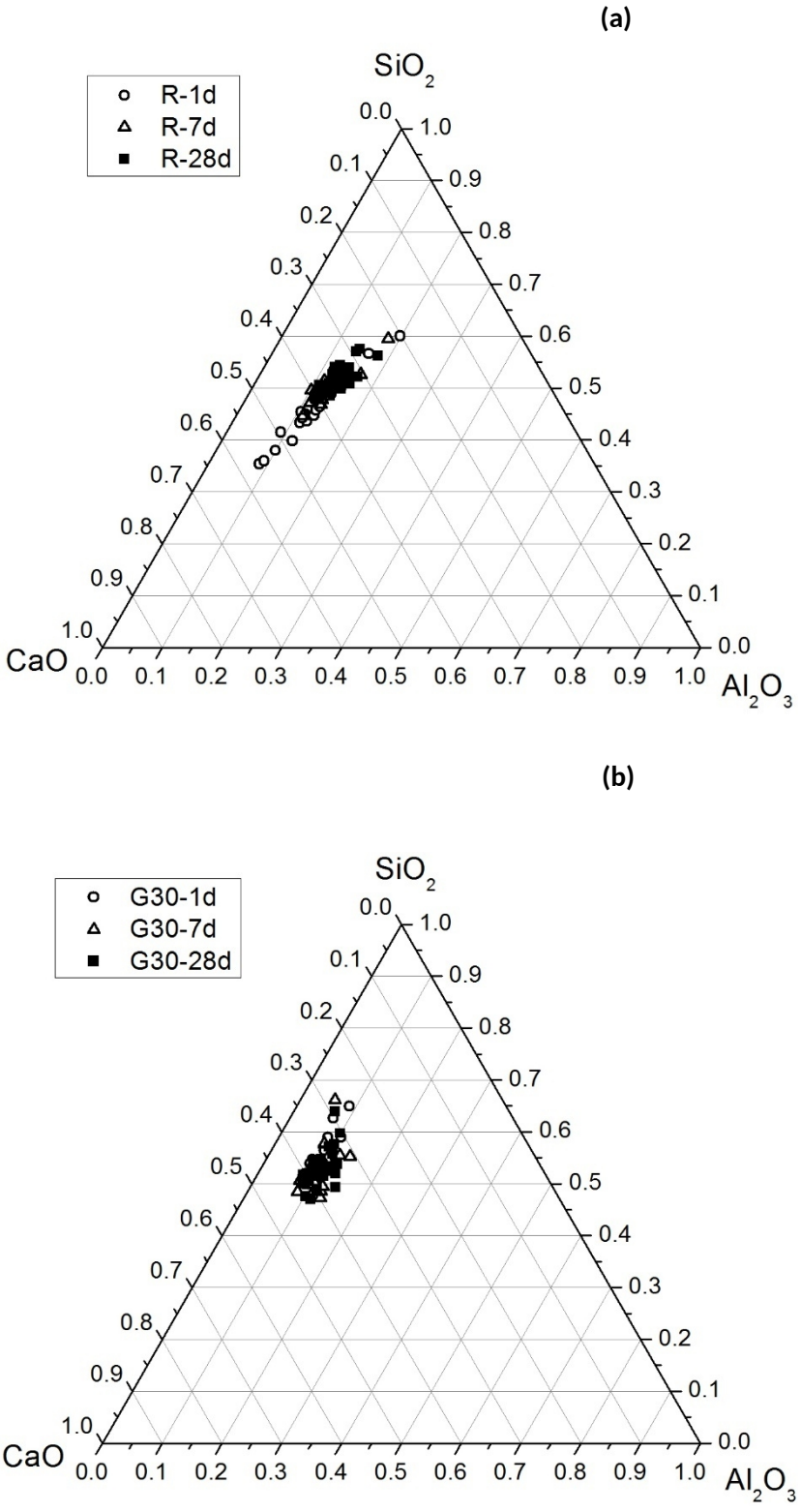

778

779 **Figure 14: Ternary diagram of EDX spot analysis of (a) R and (b) G30 mixtures cured for 1, 7,**

780 **and 28 days.**